Hydrogenated TiO_2 Thin Film for Accelerating Electron Transport in Highly Efficient Planar Perovskite Solar Cells

*Xin Yao, Junhui Liang, Yuelong Li, Jingshan Luo, Biao Shi, Changchun Wei, Dekun Zhang, Baozhang Li, Yi Ding, Ying Zhao, and Xiaodan Zhang**

Intensive studies on low-temperature deposited electron transport materials have been performed to improve the efficiency of n-i-p type planar perovskite solar cells to extend their application on plastic and multijunction device architectures. Here, a TiO_2 film with enhanced conductivity and tailored band edge is prepared by magnetron sputtering at room temperature by hydrogen doping (HTO), which accelerates the electron extraction from perovskite photoabsorber and reduces charge transfer resistance, resulting in an improved short circuit current density and fill factor. The HTO film with upward shifted Fermi level guarantees a smaller loss on V_{OC} and facilitates the growth of high-quality absorber with much larger grains and more uniform size, leading to devices with negligible hysteresis. In comparison with the pristine TiO_2 prepared without hydrogen doping, the HTO-based device exhibits a substantial performance enhancement leading to an efficiency of 19.30% and more stabilized photovoltaic performance maintaining 93% of its initial value after 300 min continuous illumination in the glove box. These properties permit the room-temperature magnetron sputtered HTO film as a promising electron transport material for flexible and tandem perovskite solar cell in the future.

1. Introduction

Lead halide perovskite materials have recently attracted intensive attention because of their unique features, such as high charge carrier mobility,[1] large absorption coefficient,[2] direct bandgap, low crystal formation energies,[3] long diffusion length,[4] and unique tolerance to structural defects.[5,6] Efficiencies over 22% have been reported since their first application in solar cells in 2009.[7] As perovskites possess long charge carrier diffusion lengths and exhibit ambipolar behavior,[8] variety of perovskite solar cell (PSC) architectures have been developed, such as the mesoporous[9–11] and planar[12–14] devices, n-i-p[15–17] and p-i-n[18–20] structures. As the planar structure has a simpler fabrication process exempt for the time consumable high temperature treatment of compact electron transport layer and/or mesoporous scaffold, substantial efforts have focused on the n-i-p planar PSCs to obtain an exceptional performance with long-term stability.

As one of the key functional layers in planar PSC devices, the compact electron transport layer (ETL) extracts and transports photogenerated electrons from the perovskite absorber and blocks generated holes transfer to fluorine doped tin oxide (FTO) substrate. A high-quality ETL, with appropriate conduction and valance band, superior electron mobility, and conductivity is crucial to achieve high efficiency of planar PSCs by reducing excessive charge accumulation and facilitating effective electron injection at the ETL/perovskite interface. TiO_2 is the most extensively employed electron collector in junction with perovskites. In order to achieve PSCs with excellent performance, high-temperature sintering is always required to increase its crystallinity for high

X. Yao, J. Liang, Prof. Y. Li, B. Shi, C. Wei, D. Zhang, B. Li, Prof. Y. Ding, Prof. Y. Zhao, Prof. X. Zhang
Institute of Photoelectronic Thin Film Devices and Technology of Nankai University
Tianjin 300071, P. R. China
E-mail: xdzhang@nankai.edu.cn

X. Yao, J. Liang, Prof. Y. Li, B. Shi, C. Wei, D. Zhang, B. Li, Prof. Y. Ding, Prof. Y. Zhao, Prof. X. Zhang
Key Laboratory of Photoelectronic Thin Film Devices and Technology of Tianjin
Tianjin 300071, P. R. China

DOI: 10.1002/advs.201700008

X. Yao, J. Liang, Prof. Y. Li, B. Shi, C. Wei, D. Zhang, B. Li, Prof. Y. Ding, Prof. Y. Zhao, Prof. X. Zhang
Key Laboratory of Optical Information Science and Technology of Ministry of Education
Tianjin 300071, P. R. China

X. Yao, Prof. Y. Zhao, Prof. X. Zhang
Collaborative Innovation Center of Chemical Science and Engineering (Tianjin)
Tianjin 300072, China

Dr. J. Luo
Laboratory for Photonics and Interfaces
Institution of Chemical Sciences and Engineering
School of Basic Sciences
Swiss Federal Institute of Technology
Lausanne CH-1015, Switzerland

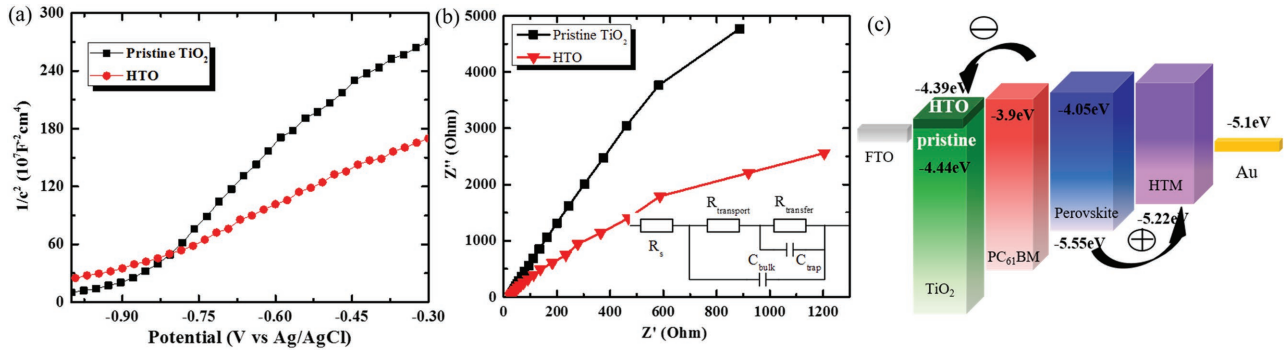

Figure 1. a) Mott–Schottky plots collected at a frequency of 5 kHz for pristine TiO_2 and HTO films. b) Nyquist plots for EIS measured at 1.6 V versus RHE of pristine TiO_2 and HTO (the inset diagram is the equivalent circuit model used to fit the Nyquist plots). c) Energy diagram for perovskite solar cells based on pristine TiO_2 and HTO films.

charge carrier mobility,[21–24] which impedes the continuous production and is also incompatible with temperature-sensitive substrates, such as plastics and substrates with multijunctions.[25]

TiO_2 films fabricated at low temperature are being ardently pursued,[26–28] and breakthrough progress has been made with the TiO_2-based PSCs compatible for flexible substrates. Yang et al. have reported a dense amorphous TiO_2 film by magnetron sputtering at room temperature, and achieved 15.07% efficiency on flexible substrates.[29] However, the poor conductivity of amorphous TiO_2 is an inherent problem, and several methods have been attempted to solve this problem. For example, graphene nanoflakes were used to modify TiO_2 films processed at 150 °C to provide superior charge collection and improve the photovoltaic performance.[30] Besides adding conductive substances to improve the conductivity, doping is another crucial strategy commonly used. For example, Y-doped TiO_2 sintered at 150 °C was utilized for better electron transport.[31] Mg-doped TiO_2 annealed at 150 °C was introduced to improve electron transfer from perovskite to TiO_2.[32] Nevertheless, investigation of room temperature fabricated TiO_2 is still urgent, which can further simplify the fabrication process and allow the continuous production especially on the cheap plastic substrates such as polyethylene terephthalate.

Hydrogen is usually used as a shallow donor and provides free carriers to enhance the conductivity. While magnetron sputtering is a versatile method to deposit uniform and compact films, ensuring full coverage to prevent shunting and leakage of currents. Herein, we present a room-temperature prepared amorphous TiO_2 film with hydrogen doping (HTO) as ETL in planar PSC through magnetron sputtering. The incorporated H provides free carriers and doubles the carrier concentration in TiO_2 for a higher conductivity. By doping hydrogen, the Fermi level of TiO_2 film shifts upward as well, leading to higher open-circuit voltage (V_{OC}) of PSC. Based on the HTO substrate, planar PSCs eventually obtain an efficiency of 19.30%, significantly higher than the one based on the pristine TiO_2 film deposited without hydrogen doping (16.58%).

2. Results and Discussion

ETL plays a vital role for the performance of PSC as the V_{OC} is determined by the difference between the Femi level (E_F) of electron and hole transport layers, and the conductivity of ETL has crucial effect on the series resistance (R_S) of the device, which affects directly the short-circuit photocurrent density (J_{SC}) and fill factor (FF). We expect that hydrogen doping will elevate the E_F of TiO_2 and increase its carrier concentration for higher conductivity.

To verify this hypothesis, electrical properties of pristine TiO_2 and HTO films are calculated from Mott–Schottky plots, as presented in **Figure 1**a. Carrier densities and flat band potential of these samples are calculated using the Equations (1) and (2), where e_0 is the electron charge, ε is the dielectric constant of TiO_2 (=170), ε_0 is the permittivity of vacuum, N_d is the donor density, and V is the applied bias at the electrode. C and A are the interfacial capacitance and active area, respectively, k is Boltzmann constant, T is the absolute temperature, and e is the electronic charge

$$N_d = \left(\frac{2}{e_0 \varepsilon \varepsilon_0}\right)\left[\frac{d(1/C^2)}{dV}\right]^{-1} \quad (1)$$

$$\frac{1}{C^2} = \frac{2}{\varepsilon \varepsilon_0 A^2 e N_d}\left(V - V_{fb} - \frac{kT}{e}\right) \quad (2)$$

The carrier concentration and flat band potentials calculated from Mott–Schottky plots are shown in **Table 1**. The carrier concentration of TiO_2 film increases from 2.25×10^{21} to 4.08×10^{21} cm^{-3} with hydrogen doping, indicating we have achieved an amorphous TiO_2 film with better conductivity, which implies faster electron transport. The flat band potential is slightly lowered with hydrogen doping, implying that the E_F shifted upward. The incorporated H acts as a shallow donor to provide free carriers, which results in an improved carrier concentration, higher electrical conductivity, and E_F. In order to confirm that hydrogen doping can improve the

Table 1. Electrical properties of pristine TiO_2 and HTO films.

TiO_2	Carrier concentration [10^{21} cm^{-3}]	Flat band potential [V vs Ag/AgCl]	$R_{transport}$ [Ω cm^2]
Pristine TiO_2	2.25	−0.95	1590
HTO	4.08	−1.00	465

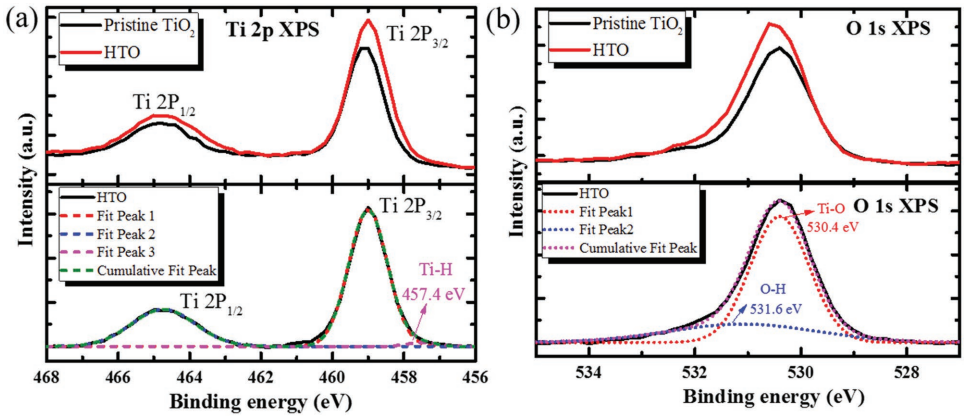

Figure 2. The experimental and fitting results of the pristine TiO_2 and HTO films: a-upper) Ti 2P XPS spetra experimental result. a-lower) The fitting result of HTO film. b-upper) Normalized O 1s XPS spectra. b-lower) The fitting result of normalized O 1s XPS spectra from HTO film.

conductivity, electrochemical impedance spectra (EIS) analyses were carried out to present the electron transport process in TiO_2. The Nyquist plots from the EIS measurements are shown in Figure 1b and the fitting results are shown in Table 1. The $R_{transport}$ in equivalent circuit model (the inset diagram in Figure 1b, the meaning of other models are presented in Characterization Methods) represents the charge transport resistance in TiO_2. A significantly reduced $R_{transport}$ of HTO indicates better conductivity, which is favorable for better performance of PSCs. The energy levels of PSC devices are presented in Figure 1c, and the energy levels are marked according to the literature.[33,34] Free charge carriers generated in the perovskite layer can be extracted by either transferring electrons to the underlying $PC_{61}BM/TiO_2$ layer, or through hole transfer to the Spiro-OMeTAD hole transport material. As the V_{OC} depends on the difference between the E_F of electron and hole transport layers, PSC based on HTO has a higher V_{OC}. In addition, the electrons can be more easily injected into the HTO film from the perovskite absorber layer due to the relative small band offset in energy levels between the conduction band of perovskite material and the Fermi level of ETL, implying a smaller loss on V_{OC} in electron transport.

To further clarify the origin of improved carrier concentration and enhanced conductivity by hydrogen doping, the X-ray photoelectron spectroscopy (XPS) spectra are analyzed to investigate the change of chemical bonding, as depicted in **Figure 2**. Comparing two samples, the Ti 2p XPS spectra are identical with Ti $2p_{3/2}$ and $2p_{1/2}$ peaks centered at binding energies of 458.9 and 464.7 eV, which are typical for the Ti^{4+}—O bonds in TiO_2,[35] while the additional broad peak centered at 457.4 eV in HTO film is attributed to the Ti—H bonds (H substitution). The Ti—H bonds passivate O vacancies and Ti dangling bonds, efficiently suppressing free charge recombination. In Figure 2b, HTO films exhibit a slight broader O 1s peaks compared to pristine TiO_2, which can be deconvoluted into two peaks centered at 530.4 and 531.6 eV. The 530.4 eV peak is typical for the Ti—O bonds in TiO_2, while 531.6 eV peak is attributed to Ti—OH bonds (H interstitial)[36,37] indicating that hydroxyl is formed through hydrogen doping. The two main bonding ways for H atom incorporated into TiO_2 films H substitution and H interstitial can both act as shallow donors to increase carrier concentration, which shifts E_F and improves the electrical conductivity, J_{SC} is therefore increased. The influence of hydrogen doping for the morphology of TiO_2 film is also analyzed through scanning electron microscope (SEM), as shown in Figure S1 in the Supporting Information. HTO film presents a smoother morphology compared with pristine TiO_2, which is beneficial for the spin-coating process of subsequent layers.

The pristine TiO_2 and HTO films are applied to planar PSC devices, whose fabrication processes are schematically depicted in **Figure 3**a, adapted from a previous report.[38] $PC_{61}BM$ layer is deposited for efficient charge extraction, making the device much less sensitive to the device polarization.[15] The surface morphology of perovskite films based on pristine TiO_2 film and HTO is presented in Figure 3b,c, respectively. With the two-step spin-coating procedure, the surface exhibits a uniform morphology with dense grains. The entire film is composed of a homogeneous, well-crystallized perovskite layer, with crystalline grains on the length scale of hundreds of nanometers. The close inspection of the surface images suggests that HTO substrate allows for a larger grain size of perovskite layer (see the statistical distribution in Figure 3d). This may be induced by the smoother morphology of HTO film, which is beneficial for the subsequent spin-coating process for the $PC_{61}BM$ and perovskite layers. The larger grain size and reduced grain boundaries may be beneficial to an increased J_{SC}. Figure 3e shows the X-ray diffraction (XRD) spectra of the prepared $(FAPbI_3)_{0.48}(MAPbI_3)_{0.52}$ films on $PC_{61}BM$/pristine TiO_2 (HTO)/FTO/glass substrates after annealing at 115 °C for 15 min. The sharp diffraction peaks prove the high crystallinity of the as-synthesized films, and its characteristic peaks are located at 14.0°, 19.8°, 24.3°, 28.3°, 31.7°, 34.7°, 40.2°, 42.9°, 50.0°, 52.1°, respectively, which is consistent with previously reported data.[9,39,40] The peak at 14.0°, 28.3°, and 31.7° corresponding to (110), (220), and (310) orientation, respectively are stronger than others, implying a preferential growth direction along these directions. The diffraction peaks of the perovskite film are stronger with the HTO substrate, suggesting better crystalline quality of perovskite.

Besides these, the time-resolved photoluminescence (TRPL) decays are measured to probe the effect of HTO on carrier dynamics in PSCs in **Figure 4**a. With global biexponential fits,

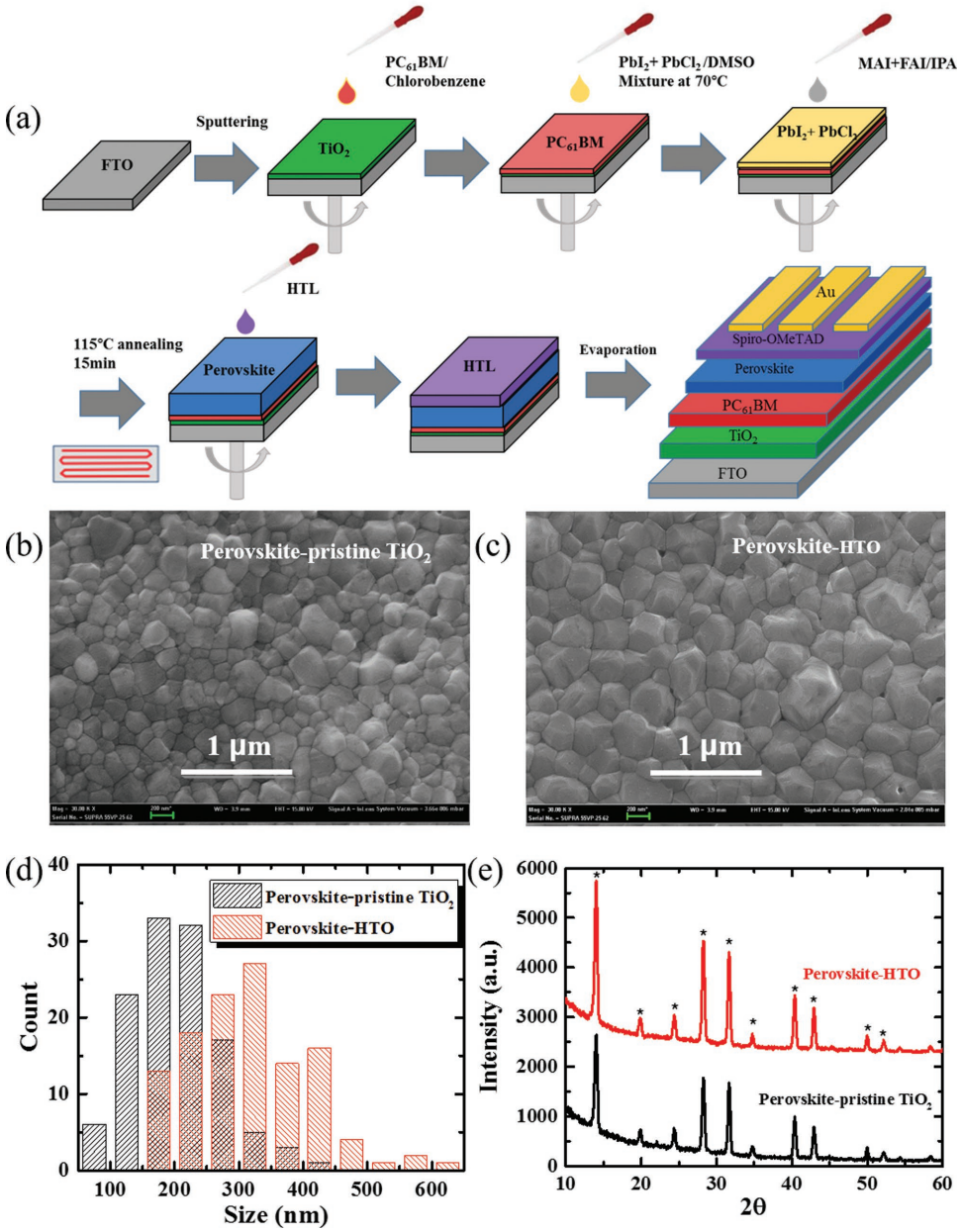

Figure 3. a) Schematic descriptions of device fabrication process. b,c) Top-view SEM images of perovskite film based on pristine TiO_2 and HTO, respectively. d) Grain sizes distribution as estimated from the SEM images using Nano measurer 1.2 software. e) X-ray diffraction spectra of PSCs based on pristine TiO_2 and HTO. Asterisks denote the perovskite phase.

the PL decay of perovskite films based on pristine TiO_2 and HTO exhibits a time-constant of τ_1 = 0.91 and 0.11 ns, respectively, which verifies the faster electron injection rate from perovskite into HTO than pristine TiO_2, resulting in a higher electron injection quantum efficiency after the electron–hole separation.[41] We ascribe it to a higher conductivity for HTO film. To further investigate the charge transport process in the devices, Nyquist plots are obtained by measuring alternating current (AC) impedance spectroscopy of the perovskite devices under an illumination of 1 sun without forward bias voltage, as shown in Figure 4b. Impedance spectroscopy measurements reveal the information on the total Ohmic resistance which is associated with the series resistance.[42,43] The semicircle corresponding to the device based on HTO is smaller than that of pristine TiO_2 film, which results from the lower internal resistance stemmed from the lower series resistance and better charge injection at the interface between HTO and perovskite material. These data predict the higher FF of the PSC based on HTO.

Figure 5a,b demonstrates the photocurrent density–voltage (J–V), external quantum efficiency (EQE) curves, and the integrated J_{SC} of planar PSCs prepared using pristine TiO_2 and HTO under simulated one sun illumination, respectively. The detail photovoltaic parameters of these devices are given in **Table 2**.

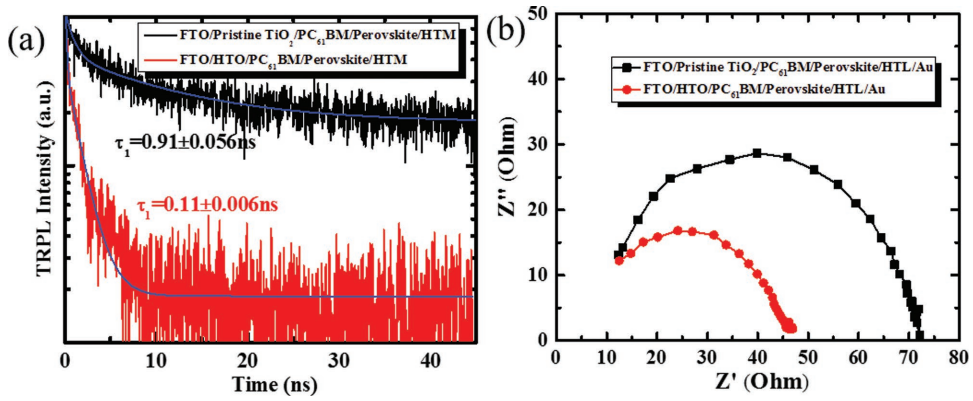

Figure 4. a) Normalized time-resolved photoluminescence of HTM/Perovskite/$PC_{61}BM$/TiO_2 deposited with and without hydrogen doping. b) Nyquist plots of PSCs based on pristine TiO_2 and HTO under 100 mW cm^{-2} AM 1.5G illumination.

The increased cell efficiency is ascribed to the enhancement of V_{OC}, J_{SC}, and FF values. From a typical cross-sectional SEM image of a real device, shown in the inset image of Figure 5a, we can see a uniform perovskite layer with 400 nm thickness, which is sufficient for the light absorption. The device exhibits distinct pin-hole free layers, avoiding the shunting and leakage of currents, which ensures a high V_{OC}. The upward shifted E_F of HTO contributes to the V_{OC} promotion. The increased FF and J_{SC} values are resulted from the reduced series resistance (R_S) due to the high conductivity of HTO and increased carrier concentration with the added donors from hydrogen doping. The accelerated electron injection rate and increased grain size and improved crystallization of perovskite film also contribute to the improved J_{SC}. Figure 5c illustrates the statistical histogram chart of device calibrated efficiency and the parameters of statistical cells are listed in Tables S1 and S2 in the Supporting Information. It demonstrates that an average efficiency of 15.48% and 18.18% can be achieved respectively for devices fabricated with pristine TiO_2 and HTO.

Figure 6a,b presents *J–V* curves of PSCs based on pristine TiO_2 and HTO obtained from forward scan (from short-circuit to open-circuit under the forward bias voltage, hereafter abbreviated as FS) and reverse scan (from open-circuit to short-circuit under the forward bias voltage, hereafter abbreviated as RS). PSC based on HTO substrate shows less hysteresis compared with the pristine TiO_2 substrate. To quantify the hysteresis effect, a modified *J–V* hysteresis index (HI) is defined as Equation (3), where $J_{RS}(V_{OC}/2)$ and $J_{FS}(V_{OC}/2)$ represent photocurrent density at 50% of V_{OC} for the reverse and forward scan, respectively.[44] The HI decreases from 0.045 to 0.008, which might be originated from the increased grain size of perovskite absorber[45] and the reduced capacitance at the interface between perovskite and ETL, as seen in Figure 3c and Figure 4b, respectively[46]

$$\mathrm{HI} = \frac{J_{RS}\left(\frac{V_{OC}}{2}\right) - J_{FS}\left(\frac{V_{OC}}{2}\right)}{J_{RS}\left(\frac{V_{OC}}{2}\right)} \quad (3)$$

The stability is another important factor in the performance of PSCs, thus it was also investigated for the PSC based on HTO. Figure 6c shows the changes of various parameters, i.e., the stability of the PSC stored in glove box at room temperature under illumination without encapsulation as a function of time. Here, the conversion efficiency decay is defined by Equation (4), where $Eff._0$ and $Eff._t$ are the efficiencies at the start and the end, respectively. The perovskite cell exhibits very stable performance, with a ΔEff. of ≈7.47% illumination after 300 min. This result is attributed to the highly crystalline properties of the perovskite absorber.

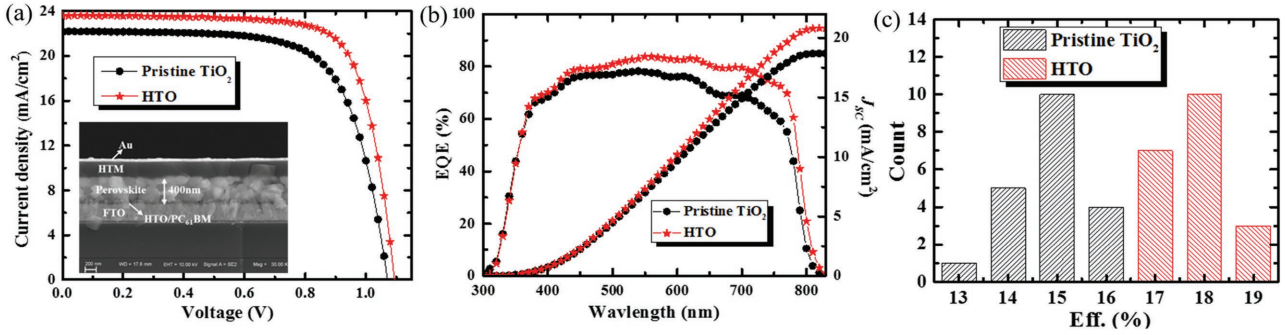

Figure 5. a) The reverse *J–V* curves of perovskite solar cells based on pristine TiO_2 and HTO films measured under simulated AM1.5 sunlight of 100 mW cm^{-2} irradiance (inset: cross section SEM image of perovskite solar cell based on HTO). b) EQE spectra and integrated J_{SC} for perovskite solar cells based on pristine TiO_2 and HTO films. c) Statistical histogram of the efficiency values among 20 devices on pristine TiO_2 and HTO.

Table 2. Parameters of perovskite solar cells based on pristine TiO_2 and HTO films.

TiO_2	Scanning direction	J_{SC} [mA cm^{-2}]	V_{OC} [V]	FF	Eff. [%]	R_S [Ω cm^2]
Pristine TiO_2	Reverse	22.19	1.07	0.70	16.58	5.35
	Forward	21.82	1.07	0.67	15.63	5.92
HTO	Reverse	23.60	1.09	0.75	19.30	4.16
	Forward	23.51	1.09	0.75	19.22	4.06

$$\Delta \mathrm{Eff}\cdot = \frac{\mathrm{Eff}_{\cdot 0} - \mathrm{Eff}_{\cdot t}}{\mathrm{Eff}_{\cdot 0}} \quad (4)$$

To determine the steady-state efficiency, the device was held at an external bias close to the maximum power point and the current was recorded under one sun illumination. As shown in Figure 6d, a stable photocurrent density of 21.1 mA cm^{-2} was observed at a bias of 0.90 V, indicating that a steady-state efficiency of the device is obtained.

3. Conclusions

In summary, we report a room-temperature prepared hydrogen doped amorphous TiO_2 film with an enhanced conductivity applied as electron transport layer in planar PSCs and obtain an efficiency of 19.30%. The incorporated H leads to an improved carrier concentration, higher electrical conductivity, and higher E_F. The improved electrical conductivity facilitates electron transport in ETL. With an elevated electron extraction rate, a higher J_{SC} is therefore obtained. The higher E_F widens the difference between the E_F of electron and hole transport layers and shortens the relative band offset in energy levels between the conduction band of perovskite and ETL, resulting in the increase of V_{OC}. Besides these, the HTO substrate is also beneficial to the crystallization of perovskite films, giving much larger grain size with more uniform size. Moreover, the HTO-based PSC exhibits negligible hysteresis and more stabilized performance. These results presented here permit the room-temperature sputtered TiO_2 film as an excellent candidate of the electron transport layer in flexible and tandem perovskite solar cells.

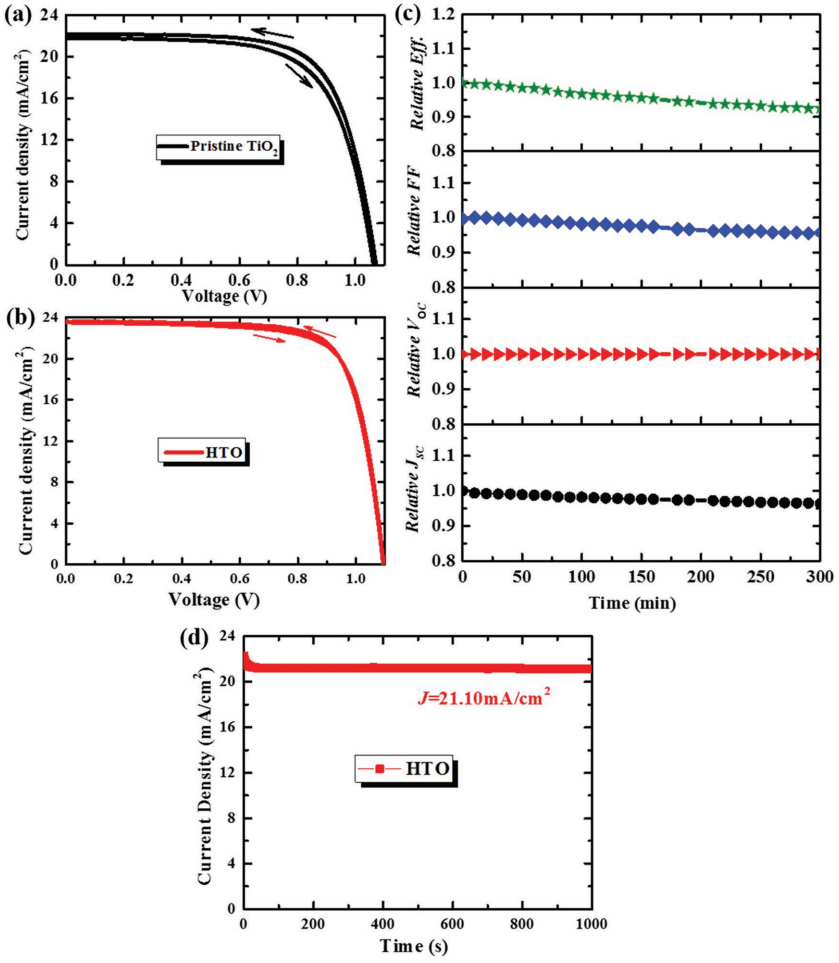

Figure 6. a) *J–V* curves including reverse and forward scan directions of PSCs based on pristine TiO_2. b) *J–V* curves including reverse and forward scan directions of PSCs based on HTO. c) Normalized parameters of PSCs based on the HTO substrate stored in glove box at room temperature without encapsulation under 100 mW cm^{-2} AM 1.5G illumination. d) Steady-state measurement of the photocurrent near the maximum power point at 0.9 V under 100 mW cm^{-2} AM 1.5G illumination.

4. Experimental Section

Device Fabrication: The FTO substrate was ultrasonically rinsed sequentially in detergent, deionized water, and finally dried under a flow of clean air. TiO_2 films were deposited on the FTO substrate using pulsed direct-current magnetron sputtering system. Intrinsic TiO_2 ceramic target (99.999%) was selected and hydrogen flow rate varied with 0 and 5 sccm. Substrate was kept at room temperature. TiO_2 film thickness was kept as a constant of 56 nm, and the TiO_2 films were used as an ETL in photoanode. A $PC_{61}BM$ (Sigma-Aldrich) buffer layer was then spin-coated above at a speed of 3500 rpm for 30 s.

Deposition of perovskite film was performed using sequential method: 1.6 M $PbCl_2$ (Sigma-Aldrich) and PbI_2 (Sigma-Aldrich) ($PbCl_2$:PbI_2 molar ratio 1:1) dissolved in the dimethyl sulfoxide (DMSO) (Tianjin Guangfu Fine Chemical Research Institute) solvent (keeping at 70 °C) were spin casted on $PC_{61}BM$ layer at 3000 rpm for 60 s, with the film dried at room temperature. Then, 200 µL of methylammonium iodide (MAI) and formamidinium iodide (FAI) (Shanghai Mater. Win. New Materials Corporation) mixed solution dissolved in isopropanol (20 mg mL^{-1}, weight ratio 1:1) was loaded on the prepared film for 2 min before spin-coating at 3000 rpm for 60 s, and then sample was annealed at 115 °C for 15 min. The thickness of perovskite film is ≈400 nm.

The organic hole transporting layer was prepared by dissolving 80 mg Spiro-OMeTAD (1 material), 28.5 µL 4-tert-Butylpyridine (TBP) (Aladdin Reagents), and 17.5 µL LiTFSI (Aladdin Reagents) solution (520 mg Li-TFSI in 1 mL acetonitrile) in 1 mL chlorobenzene (Aladdin Reagents), and spin casted on the perovskite film at 6000 rpm for 60 s. Finally, gold electrode was thermally evaporated on the top through a shadow mask. Except for electrode evaporation, all fabrication processes were completed in a nitrogen filled glove box. Fabricated devices were stored under dry conditions

without sealing and measured in normal ambient atmosphere with the circumstance temperature of 25 °C.

Characterization Methods: Film crystal structure of perovskite was examined by XRD spectra (a Rigaku, ATX-XRD) with Cu Kα radiation (λ = 0.154 nm) in the 2θ range from 10° to 60°. The morphologies of the solar cells were tested using a SEM (Jeol JSM-6700F). The TRPL spectroscopy was measured with a PL spectrometer (Edinburgh Instruments, FLS 920), and a pulsed laser with a wavelength and frequency of 635 nm and 1 MHz was employed as the excitation source. A long pass filter of 655 nm was used to filter out the excitation light in the transient PL measurements. The Ti 2p and O 1s core peaks were detected using XPS (PHI5000VersaProbe). EIS of the TiO_2 films were performed in a three-electrode configuration immersed in a 1 M NaOH aqueous solutions by a Princeton potentiostat electrochemical workstation (PARSTAT 4000), which contains a Pt counter electrode, an Ag/AgCl reference electrode, and TiO_2 as work electrode. The equivalent circuit model consists of a series R_S resistance representing the capacity of charge transport in the FTO substrate and external circuit, $R_{transport}$ representing charge transport resistance in TiO_2, R_{ct} representing the charge transfer resistance at the interface between the semiconductor and electrolyte. Herein, we mainly focus on the $R_{transport}$. EIS of the perovskite solar cells was performed on a PARSTAT 4000 in AM 1.5G in the frequency ranging from 1 Hz to 1 MHz without a bias.

Photovoltaic Characterization: Photocurrent density–voltage (*J*–*V*) curves of solar cells were measured at 25 °C under the AM 1.5G (100 mW cm^{-2}) illumination. A metal mask with a window of 0.1 cm^2 was clipped on light injection side to define the active area of the cell. Unless specified, bias scan from 1.2 to −0.2 V first (reverse scan) and return back (forward scan) with a voltage step of 20 mV and delay time 50 ms. Reverse curve is mainly adopted to evaluate the device performance. The spectral response was taken by an EQE measurement system (QEX10, PV Measurement).

Supporting Information

Supporting Information is available from the Wiley Online Library or from the author.

Acknowledgements

The authors gratefully acknowledge the supports from International Cooperation Project of the Ministry of Science and Technology (Grant No. 2014DFE60170), National Natural Science Foundation of China (Grant Nos. 61474065 and 61674084), Tianjin Research Key Program of Application Foundation and Advanced Technology (Grant No. 15JCZDJC31300), Key Project in the Science & Technology Pillar Program of Jiangsu Province (Grant No. BE2014147-3), and the 111 Project (Grant No. B16027).

Conflict of Interest

The authors declare no conflict of interest.

Keywords

electron transport layer, faster electron transport behavior, hydrogen doping, planar perovskite solar cells, room temperature magnetron sputtering process

Received: January 9, 2017
Revised: February 26, 2017
Published online: May 16, 2017

[1] C. S. Ponseca Jr., T. J. Savenije, M. Abdellah, K. Zheng, A. Yartsev, T. R. Pascher, T. Harlang, P. Chabera, T. Pullerits, A. Stepanov, *J. Am. Chem. Soc.* **2014**, *136*, 5189.
[2] S. De Wolf, J. Holovsky, S.-J. Moon, P. Löper, B. Niesen, M. Ledinsky, F.-J. Haug, J.-H. Yum, C. Ballif, *J. Phys. Chem. Lett.* **2014**, *5*, 1035.
[3] H. S. Jung, N.-G. Park, *Small* **2015**, *11*, 10.
[4] S. D. Stranks, G. E. Eperon, G. Grancini, C. Menelaou, M. J. Alcocer, T. Leijtens, L. M. Herz, A. Petrozza, H. J. Snaith, *Science* **2013**, *342*, 341.
[5] Y.-J. Jeon, S. Lee, R. Kang, J.-E. Kim, J.-S. Yeo, S.-H. Lee, S.-S. Kim, J.-M. Yun, D.-Y. Kim, *Sci. Rep.* **2014**, *4*, 1312.
[6] W.-J. Yin, T. Shi, Y. Yan, *Appl. Phys. Lett.* **2014**, *104*, 063903.
[7] NREL efficiency chart, http://www.nrel.gov/ncpv/images/efficiency_chart.jpg (accessed: November, 2016).
[8] J. M. Ball, M. M. Lee, A. Hey, H. J. Snaith, *Energy Environ. Sci.* **2013**, *6*, 1739.
[9] J. Burschka, N. Pellet, S. J. Moon, R. Humphry-Baker, P. Gao, M. K. Nazeeruddin, M. Grätzel, *Nature* **2013**, *499*, 316.
[10] C. Y. Yi, X. Li, J. S. Luo, S. M. Zakeeruddin, M. Gratzel, *Adv. Mater.* **2016**, *28*, 2964.
[11] A. J. Pearson, G. E. Eperon, P. E. Hopkinson, S. N. Habisreutinger, J. T. W. Wang, H. J. Snaith, N. C. Greenham, *Adv. Energy Mater.* **2016**, *6*, 1600014.
[12] M. Z. Liu, M. B. Johnston, H. J. Snaith, *Nature* **2013**, *501*, 395.
[13] Y. Liu, M. Bag, L. A. Renna, Z. A. Page, P. Kim, T. Emrick, D. Venkataraman, T. P. Russell, *Adv. Energy Mater.* **2016**, *6*, 1501606.
[14] C.-W. Chen, H.-W. Kang, S.-Y. Hsiao, P.-F. Yang, K.-M. Chiang, H.-W. Lin, *Adv. Mater.* **2014**, *26*, 6647.
[15] C. Tao, S. Neutzner, L. Colella, S. Marras, A. R. Srimath Kandada, M. Gandini, M. D. Bastiani, G. Pace, L. Manna, M. Caironi, C. Bertarelli, A. Petrozza, *Energy Environ. Sci.* **2015**, *8*, 2365.
[16] H. Zhang, J. Mao, H. X. He, D. Zhang, H. L. Zhu, F. X. Xie, K. S. Wong, M. Grätzel, W. C. H. Choy, *Adv. Energy Mater.* **2015**, *5*, 1501354.
[17] Z. C. Yuan, Z. W. Wu, S. Bai, Z. H. Xia, W. D. Xu, T. Song, H. H. Wu, L. H. Xu, J. J. Si, Y. Z. Jin, B. Q. Sun, *Adv. Energy Mater.* **2015**, *5*, 1500038.
[18] Q. F. Xue, G. T. Chen, M. Y. Liu, J. Y. Xiao, Z. M. Chen, Z. C. Hu, X. F. Jiang, B. Zhang, F. Huang, W. Yang, H. L. Yip, Y. Cao, *Adv. Energy Mater.* **2016**, *6*, 1502021.
[19] D. W. Zhao, M. Sexton, H. Y. Park, G. Baure, J. C. Nino, F. So, *Adv. Energy Mater.* **2015**, *5*, 1401855.
[20] C. Sun, Z. H. Wu, H. L. Yip, H. Zhang, X. F. Jiang, Q. F. Xue, Z. C. Hu, Z. H. Hu, Y. Shen, M. K. Wang, F. Huang, Y. Cao, *Adv. Energy Mater.* **2016**, *6*, 1501534.
[21] B. S. Ong, C. Li, Y. Li, Y. Wu, R. Loutfy, *J. Am. Chem. Soc.* **2007**, *129*, 2750.
[22] L. Zuo, Z. Gu, T. Ye, W. Fu, G. Wu, H. Li, H. Chen, *J. Am. Chem. Soc.* **2015**, *137*, 2674.
[23] Y. Shih, L. Wang, H. Hsieh, K. Lin, *J. Mater. Chem. A* **2015**, *3*, 9133.
[24] Y. Ogomi, A. Morita, S. Tsukamoto, T. Saitho, Q. Shen, T. Toyoda, K. Yoshino, S. S. Pandey, T. Ma, S. Hayase, *J. Phys. Chem. C* **2014**, *118*, 16651.
[25] Z. M. Beiley, M. D. McGehee, *Energy Environ. Sci.* **2012**, *5*, 9173.
[26] K. Yamamoto, Y. Zhou, T. Kuwabara, K. Takahashi, M. Endo, A. Wakamiya, Y. Ogomi, S. Hayase, T. Taima, presented at *PVSC 2014*, Danver, Colorado, USA, June, **2014**.
[27] W. M. Qiu, U. W. Paetzold, R. Gehlhaar, V. Smirnov, H. G. Boyen, J. G. Tait, B. Conings, W. M. Zhang, C. B. Nielsen, I. McCulloch, L. Froyen, P. Heremans, D. Cheyns, *J. Mater. Chem. A* **2015**, *3*, 22824.
[28] B. Conings, L. Baeten, T. Jacobs, R. Dera, J. D'Haen, J. Manca, H. G. Boyen, *Appl. Mater.* **2014**, *2*, 081505.

[29] D. Yang, R. Yang, J. Zhang, Z. Yang, S. Liu, C. Li, *Energy Environ. Sci.* **2015**, *8*, 3208.
[30] J. T. W. Wang, J. M. Ball, E. M. Barea, A. Abate, J. A. Alexander-Webber, J. Huang, M. Saliba, I. Mora-Sero, J. Bisquert, H. J. Snaith, R. J. Nicholas, *Nano Lett.* **2014**, *14*, 724.
[31] H. Zhou, Q. Chen, G. Li, S. Luo, T. B. Song, H. S. Duan, Z. Hong, J. You, Y. Liu, Y. Yang, *Science* **2014**, *345*, 542.
[32] J. Wang, M. C. Qin, H. Tao, W. J. Ke, Z. Chen, J. W. Wan, P. L. Qin, L. B. Xiong, H. W. Lei, H. Q. Yu, G. J. Fang, *Appl. Phys. Lett.* **2015**, *106*, 091102.
[33] J. Liang, H. Tan, M. Liu, B. Liu, N. Wang, Q. Zhang, Y. Zhao, A. H. M. Smets, M. Zeman, X. Zhang, *J. Mater. Chem. A* **2016**, *4*, 16841.
[34] P. Gao, M. Gratzel, M. K. Nazeeruddin, *Energy Environ. Sci.* **2014**, *7*, 2448.
[35] M. Lazarus, T. Sham, *Chem. Phys. Lett.* **1982**, *92*, 670.
[36] A. Janotti, C. G. Van de Walle, *Nat. Mater.* **2007**, *6*, 44.
[37] E. McCafferty, J. Wightman, *Surf. Interface Anal.* **1998**, *26*, 549.
[38] J.-H. Im, I.-H. Jang, N. Pellet, M. Grätzel, N.-G. Park, *Nat. Nanotechnol.* **2014**, *9*, 927.
[39] Q. Jiang, L. Zhang, H. Wang, X. Yang, J. Meng, H. Liu, Z. Yin, J. Wu, X. Zhang, J. You, *Nat. Energy* **2016**, *2*, 16177.
[40] B. Slimi, M. Mollar, I. B. Assaker, I. Kriaa, R. Chtourou, B. Marí, *Energy Procedia* **2016**, *102*, 87.
[41] Y. Yang, K. Ri, A. Mei, L. Liu, M. Hu, T. Liu, X. Li, H. Han, *J. Mater. Chem. A* **2015**, *3*, 9103.
[42] H.-S. Kim, I. Mora-Sero, V. Gonzalez-Pedro, F. Fabregat-Santiago, E. J. Juarez-Perez, N.-G. Park, J. Bisquert, *Nat. Commun.* **2013**, *4*, 2242.
[43] V. Gonzalez-Pedro, E. J. Juarez-Perez, W.-S. Arsyad, E. M. Barea, F. Fabregat-Santiago, I. Mora-Sero, J. Bisquert, *Nano Lett.* **2014**, *14*, 888.
[44] R. S. Sanchez, V. Gonzalez-Pedro, J.-W. Lee, N.-G. Park, Y. S. Kang, I. Mora-Sero, J. Bisquert, *J. Phys. Chem. Lett.* **2014**, *5*, 2357.
[45] H.-S. Kim, N.-G. Park, *J. Phys. Chem. Lett.* **2014**, *5*, 2927.
[46] H. S. Kim, I. H. Jang, N. Ahn, M. Choi, A. Guerrero, J. Bisquert, N.-G. Park, *J. Phys. Chem. Lett.* **2015**, *6*, 4633.